1 **Real-time probabilistic seismic hazard assessment based on seismicity anomaly**

2

3 Yu-Sheng Sun[1*], Hsien-Chi Li[1], Ling-Yun Chang[1], Zheng-Kai Ye[1], and Chien-Chih Chen[1, 2]

4 [1]Department of Earth Sciences, National Central University, Taoyuan City 32001, Taiwan, R.O.C.

5 [2]Earthquake-Disaster and Risk Evaluation and Management Center, National Central University,

6 Taoyuan City 32001, Taiwan, R.O.C.

7 Correspondence: Yu-Sheng Sun (sheng6010@gmail.com)

8

9 **Abstract**

10 The real-time Probabilistic Seismic Hazard Assessment (PSHA) is developed for considering the

11 practicability for daily life and the rate of seismic activity with time. The real-time PSHA follows

12 the traditional PSHA framework, but the statistic occurrence rate is substituted by time-dependent

13 seismic source probability. Pattern Informatics method (PI) is a proper time-dependent probability

14 model of seismic source, which have been developed over a decade. Therefore, in this research,

15 we chose the PI method as the function of time-dependent seismic source probability and selected

16 two big earthquakes in Taiwan, the 2016/02/05, Meinong earthquake (M_L 6.6) and the 2018/02/06,

17 Hualien earthquake (M_L 6.2), as examples for the real-time PSHA. The forecasting seismic

18 intensity maps produced by the real-time PSHA present the maximum seismic intensity for the

19   next 90 days. Compared to real ground motion data from the P-alert network, these forecasting

20   seismic intensity maps have considerable effectiveness in forecasting. It indicates that the real-

21   time PSHA is practicable and can provide a useful information for the prevention of earthquake

22   disasters.

23

24   **1   Introduction**

25   At present, there are two major phases about the researches and applications of seismic hazard: the

26   pre-earthquake and the post-earthquake. The most important usage of the post-earthquake seismic

27   hazard assessment is the Earthquake Early Warning (EEW) system (Cooper, 1868; Wu et al., 1998;

28   Wu et al., 2013). It provides extra time for people to take refuge before the larger seismic wave

29   arrives. On the other hand, Probabilistic Seismic Hazard Analysis (PSHA; Cornell, 1968; SSHAC,

30   1997) is the most common methodology of the pre-earthquake seismic hazard assessment and

31   mainly for engineering design. PSHA determines the exceeding probability of ground motion level

32   over a specified time period based on the occurrence rate of earthquake and ground motion

33   prediction equations (GMPEs). The occurrence rate of earthquake is generally described by the

34   truncated exponential model (Cosentino et al., 1977) and the characteristic earthquake model

35   (Schwartz and Coppersmith, 1984; Wang et al., 2016). No matter the data is from long-term

36   observations or paleoseismic studies, the earthquake occurrence rate computed from these models

37   will not change with time. However, the seismic activity is a complex dynamic process in time and

38   space and usually fluctuates enormously in short time scale (Chen et al., 2006). Furthermore, the

39   assessment is usually computed by using very long recurrence interval, 475 or 2475 years, for the

40   purpose of engineering design (Iervolino et al., 2011). As a result, it is hard to verify the accuracy

41   of seismic hazard assessment in limited life because of such long period. On the other hand, such

42   long interval is suitable for buildings, but not for human's life which is definitely much shorter

43   than the life span of buildings. In other words, the concept of catastrophic in such long recurrence

44   intervals is difficult to resonate in the daily life of general public. In addition, the definition like

45   10% probability in 50 years is hard to image for most ordinary people. Therefore, a statistical long-

46   term seismic hazard assessment is useless in our daily life. On the contrary, we believe that a short-

47   term and time-dependent pre-earthquake hazard assessment is necessary for everyone's daily use.

48   In this study, we suggested a preliminary method to achieve this goal by using a time-dependent

49   seismic source probability instead of the static one in the long-term assessment. One of the capable

50   candidates as a time-dependent seismic source probability is the Pattern Informatics (PI) method,

51   which has developed over the past decade (Rundle et al., 2000; Tiampo et al., 2002; Wu et al.,

52   2008a; Chang et al., 2016).

53

54   Anomalous change in seismicity is widely used as precursory indicator for big earthquakes and is

55   usually classified into seismic activation or seismic quiescence, depending on ascending or

56   descending number or occurrence rate of seismicity (Chen et al., 2005; Wu et al., 2008b). In the

57   PI method, big earthquakes tend to occur after precursory anomalous seismic changes and its

58   occurrence probability can be quantified by the magnitude of spatiotemporal variation of

59   seismicity. In preliminary researches, PI performs good in identifying locations nearby upcoming

60   big earthquakes. A modified version of PI developed in the recent researches has obviously

61   improved the accuracy of identifying occurrence time interval of big earthquakes. The occurrence

62   probability of big earthquakes in the next 90 days is plausible after a series of verification (Chang

63   et al., 2016; Chang, 2018). Therefore, we used the modified PI method to compute the time-

64   dependent seismic source probability of each location while the area of interest is coarse-grained

65   by square in uniform size.

66

67   In this research, we illustrate a simple way to achieve a real-time seismic hazard assessment. The

68   crucial step is to replace statistical seismic probability by the time-dependent probability from the

69   modified PI method. The real-time seismic hazard assessment produced the seismic hazard

70   forecasting maps for the next 90 days. The "real-time" PSHA can be updated with earthquake

71   catalog refreshing (time-dependent) and forecast for the near future (short-term), and compared

72   with the forecasting time scale and static seismic rate of the traditional PSHA, these can be called

73   "real-time". We illustrated this real-time assessment process by two recent big earthquakes in

74   Taiwan, the 2016 Meinong earthquake (M_L 6.6) (Lee et al., 2016; Chen et al., 2017; Lee et al.,

75   2017) and the 2018 Hualien earthquake (M_L 6.2) (Hsu et al., 2018). Detailed parameters about

76   these two earthquakes are listed in Table 1. Finally, the reliability of the seismic hazard maps was

77   verified by comparing with real ground motion data recorded by the P-alert network.

78

79   **2   Data**

80   **2.1 Central Weather Bureau Seismic Network (CWBSN) catalog**

81   We used the CWBSN catalog maintained by the Central Weather Bureau (CWB), Taiwan

82   (https://www.cwb.gov.tw/V7e/earthquake/seismic.htm   and   http://gdms.cwb.gov.tw/index.php,

83   last access: July 2018). The completeness magnitude (M_c) of this catalog is estimated

84   approximately 2.0 in local magnitude (M_L) (Wu et al., 2008c). In the analysis of focal depth, Wu

85   et al. (2008b) showed that the focal depth for about 80% earthquakes is shallower than 30 km.

86   Therefore, we used M_L 2.0 and 30 km as the threshold of magnitude and focal depth to select

87   earthquakes used in the PI calculation.

88

89   **2.2 P-alert network**

90   In this research, the ground motion recordings from the P-alert network were used to verify the

Natural Hazards
and Earth System
Sciences

Discussions

91   effectiveness of the real-time seismic hazard assessments from our idea. The EEW research group

92   of the National Taiwan University (NTU) have begun to set up the P-alert real-time strong-motion

93   network since 2010. The device of the P-alert network can record real-time acceleration signals in

94   three-component and publish alerts if the peak initial-displacement amplitude (Pd) or peak ground

95   acceleration (PGA) exceeds a redefined threshold (Wu et al., 2013, 2016b). Nowadays, there are

96   more than 600 stations in Taiwan; most of them are located in elementary schools (Wu et al., 2013;

97   Yang et al., 2018). We mainly adopted the P-alert waveform database maintained by Taiwan

98   Earthquake research Center (TEC) and the data from NTU were as an auxiliary catalog (The data

99   of   the   P-alert   network   can   be   downloaded   from   the   Data   Center   of   TEC:

100   http://palert.earth.sinica.edu.tw/db/ (last access: July 2018) or contact with Prof. Yih-Min Wu at

101   NTU for NTU's catalog: drymwu@ntu.edu.tw). However, even if there are so many stations

102   covering Taiwan, the distribution of the P-alert network is still nonuniform (see Fig. 2b and 3b).

103   This nonuniform distribution may causes some problems that we will discuss later.

104

105   **3   Method**

106   **3.1 Pattern Informatics (PI)**

107   The physical fundamental of the PI method is phase dynamics which describes changes of a system

108   by rotation of state vector in the Hilbert space (Rundle et al., 2002; 2003). The evolution of state

Natural Hazards
and Earth System
Sciences
Discussions
Open Access
EGU

109   vector in a dynamic fault system is suggested to be related to stress accumulation and release (Chen

110   et al., 2006). The computation steps we addressed here are a modified version developed by Chang

111   et al. (2016) and Chang (2018) to improve temporal resolution of PI. The research area (119°~123°

112   E 21°~26° N) is divided into boxes of grid size 0.1°×0.1°, and each box is indicated by parameter

113   x_i. Because of the M_c and the distribution of focal depth (mentioned in Section 2.1), all events

114   having $M_L \geq 2.0$ and depth ≤ 30 km were used. In the PI computation, t_1 and t_2 are the beginning

115   and end of a change interval, respectively, and the length of change interval is 4 years. The

116   beginning time of calculation, t_0, is defined as 12 years before t_2. Then, t_b is a sampling

117   reference time between t_0 and t_1 which shifts t_b each time. The forecasting interval, t_3, starts

118   after t_2. According to Chang et al. (2016), the forecasting interval of the PI method reaches 90

119   days. Lastly, the PI method produces a forecasting probability distribution of seismic sources for

120    $M_L \geq 5.0$ within the forecasting interval.

121

122   **3.2 Real-time PSHA**

123   In the traditional PSHA framework (Cornell, 1968; Wang et al., 2016), the probability of an

124   earthquake's occurrence follows the Poisson process and the average recurrence interval for an

125   annual frequency of exceedance can be expressed as

Natural Hazards
and Earth System
Sciences
Discussions
Open Access
EGU

126
$$v(Z > z) = \sum_{i=1}^{N_S} \dot{N}_i \iint f_{M_i}(m)\, f_{R_i}(r)\, P(Z > z \mid m, r)\, dm\, dr$$

127 (1)

128 where $f_{M_i}(m)$ and $f_{R_i}(r)$ are the probability density functions of magnitude and distance,

129 respectively; $P(Z > z \mid m, r)$ is the conditional probability of ground motion Z exceeding a

130 specified value z for a specific magnitude m and distance r. $\dot{N}_i$ is the annual occurrence rate

131 of earthquakes and described by the truncated exponential model (Cosentino et al., 1977) and the

132 characteristic earthquake model (Schwartz and Coppersmith, 1984). Finally, to consider all

133 scenarios, the total probability of N_s earthquakes is summarized in a given region.

134

135 In the real-time PSHA, the occurrence rate of earthquake used in the traditional PSHA framework

136 is replaced by seismic forecasting probability to achieve spatiotemporal variability of the hazard

137 assessment. Then, considering the gridded space, the real-time PSHA can be expressed as

138
$$v(Z > z) = \sum^{M_S} \sum^{Loc_S} P_{M_i, Loc_i}(m, loc)\, P(Z > z \mid m, loc)$$

139 (2)

140 where $P_{M_i, Loc_i}(m, loc)$, the forecasting probability distribution, is a function of magnitude and

141 location. It specifies an occurrence probability for specific magnitude, M_i, at each spatial location,

142 Loc_i. The summations are to consider the whole of the contribution from any possible magnitude,

143   M_s, and location, Loc_s. In this research, we adopted the forecasting probability from the PI method

144   as $P_{M,Loc}(m, loc)$. Loc refers to x_i in the PI method. The forecasting probability of the PI

145   method presents a distribution of cumulative forecasting probability for $M_L \geq 5.0$. Thus, we

146   referred to the average character of Gutenberg-Richter law in Taiwan (Gutenberg and Richter,

147   1944; Wang et al., 2015) to turn it into probability density function (PDF). It can be corresponded

148   to the specific magnitude conditions for $P(Z > z \mid m, loc)$. To evaluate the ground motion, we

149   used the GMPE published by Lin et al. (2012), which was also adopted for the issue of Taiwan

150   PSHA in Lee et al. (2017). In this GMPE, the earthquake type is one of the important parameters.

151   However, the divisions of seismic source in the PI method is no longer based on the geological

152   classification, but the grid box, x_i. Considering that the most faults in Taiwan are reverse faults

153   (Shyu et al., 2016), we adopted the reverse fault parameters setting for the entire research area.

154   Finally, the forecasting maximum PGA from the real-time PSHA is transferred to seismic intensity

155   according to the seismic intensity scale of CWB listed in Table 2 (Wu et al., 2003). It means that

156   the forecasting seismic intensity map presents the maximum seismic intensity which every site

157   will encounter in the following 90 days.

158

159   **3.3 Performance verification**

160   **3.3.1 Receiver Operating Characteristic curve (ROC)**

Natural Hazards
and Earth System
Sciences
Discussions
EGU
Open Access

161   The ROC diagram is a binary classification model and widely used as a tool for quantifying the

162   performance of earthquake prediction (Holliday et al., 2006; Nanjo et al., 2006; Wu et al., 2016a).

163   We used the ROC diagram as an objective quantitative indicator to evaluate the performance of

164   the forecasting seismic probability computed by the PI method. For each box x_i, there are four

165   situations, parameters, while comparing forecasting hotspot and target earthquake: a means any

166   target earthquake in a hotspot; b means no target earthquake in a hotspot; c means no hotspot

167   but with at least one target earthquake; d means no target earthquake and no hotspot. True

168   positive rate (TPR) is defined as $a/(a + c)$ and false positive rate (FPR) is defined as $b/(b + d)$.

169   The values of a, b, c, and d change with threshold of forecasting probability, and therefore

170   TPR and FPR change as well. The area under the ROC curve (AUC) is between 0 and 1. AUC=1

171   is a perfect prediction; AUC=0.5 is a random guess. For each forecasting map of PI, we generated

172   1000 random tests by re-distributing the hotspots randomly over the research area to examine the

173   possibility that a specific distribution of hotspots can generate by chance. In Fig. 1c and 1d, the

174   blue line is the 95% confidence interval based on two standard deviations. The standard deviation

175   is calculated by the random test results in each bin of the x-axis. The 95% confidence interval helps

176   us differentiate the distributing range of random tests and the significant of forecasting probability.

177

178   **3.3.2   Average Percent Hit Rate (APHR)**

Natural Hazards
and Earth System
Sciences
Discussions

Open Access

EGU

179   The success rate of forecasting seismic intensity is a predictive accuracy of classification problems

180   for which the average percent hit rate (APHR) is arguably the most intuitive measure of

181   discrimination. The APHR is a rate at which the forecasting data are classified into the correct

182   classes (Sharda and Delen, 2006). In this research, the APHR was used to quantify the forecasting

183   performance of the real-time seismic hazard assessments. In the APHR, the exact hit rate which

184   only counts the correct classifications to the exact same class can be expressed as:

185     $$\text{APHR}_{\text{exact}} = \frac{1}{N} \sum_{i=1}^{g} p_i$$

186   (3)

187   where, in our case, N is the total number of the P-alert stations or the boxes on the forecasting

188   hazard map, g is the total number of seismic intensity classes (=8, according to the CWB's

189   seismic intensity scale), and p_i is the total number of samples classified as class i. In the random

190   test, we further generated 1000 random tests by randomly re-distributing the forecasting maximum

191   seismic intensity over the research area and the stations to examine the possibility that a specific

192   distribution of the forecast can generate by chance.

193

194   **4   Results**

195   **4.1 Forecast of earthquake occurrences**

196   Figure 1a and 1b show the forecasting probability maps computed by the PI method, and Fig. 1c

197   and 1d are corresponding forecasting performance verified by the ROC tests. In the case of 2016

198   Meinong earthquake, t_0, t_1, and t_2 are 2004/01/31, 2012/01/31, and 2016/01/31. In the case of

199   2018 Hualien earthquake, t_0, t_1, and t_2 are 2006/01/31, 2014/01/31, and 2018/01/31. The

200   forecasting intervals of both cases are 90 days after t_2. Cyan star in Fig. 1a and 1b is the main

201   shock of 2016 Meinong and 2018 Hualian earthquakes, and the biggest earthquake in the

202   forecasting interval. Gray circles in Fig. 1a and 1b are the earthquakes with magnitude $M_L \geq 5.0$

203   in the forecasting interval, and more detailed information about these earthquakes can be obtained

204   in Table 1. A notable point is that both main shocks and most big earthquakes are located in or

205   very close to the hotspots. The performance of the PI forecasting probabilities seems to be good

206   simply by visual inspection.

207

208   In Fig. 1c and 1d, red curves are far above the blue curves (95% confidence interval). The AUCs

209   of red curves are 0.91 and 0.94, and are apparently larger than the AUCs of blue curves, which are

210   0.73 and 0.70. The ROC tests verified quantitatively that the performance of the PI forecasting

211   probability is significant, and these patterns are not just generated by random distribution of

212   hotspots by chance. Both distributions of hotspot are physically meaningful. Therefore, we can use

213   these probability maps as the function of earthquake occurrence rate in subsequent calculation for

214   the real-time PSHA.

215

216   **4.2 Real-time PSHA**

217   In Fig. 2 and 3, panel (a) shows the map of forecasting max seismic intensity estimated by the real-

218   time PSHA for the forecasting interval; panel (b) shows the map of max seismic intensity recorded

219   by the P-alert network during the forecasting interval. To ensure that it is absolutely maximum

220   intensity during the forecasting interval, we only used the stations which have recorded all the

221   target events ($M_L \geq 5.0$) in the forecasting interval. Although there are over 600 P-alert stations

222   distributing widely in Taiwan, some boxes still do not contain any station, for example, the Central

223   Mountain Range (see Fig. 5a and 5b). Therefore, we had to estimate the intensities in such kind of

224   boxes by interpolating. Thus, this strategy indeed generates the artificial effect and we will show

225   it later.

226

227   Comparing Fig. 2a and 2b, we suggest that both seismic intensity distributions are very similar.

228   An apparent deviation of forecasting seismic intensities from the recorded values is in the

229   southwestern Taiwan, especially the area closer to the 2016 Meinong main shock. Fig. 2c shows

230   the difference of intensity between Fig. 2a and 2b; the color of blue and red means that the

231   forecasting value in a box is underestimated or overestimated. Most boxes have intensity

232   difference in the range -1 to 1, but some boxes in the southwestern Taiwan are underestimated; the

233   differences are most 2 or even up to 3.

234

235   Comparing Fig. 3a and 3b, we suggest that both seismic intensity distributions are still very similar.

236   In this case, an apparent deviation of forecasting seismic intensities from the recorded values is in

237   the southern Taiwan and a part of southwestern area. Figure 3c shows that most boxes in the

238   southern Taiwan have smaller recorded intensity, and the recorded intensities in a part of

239   southwestern Taiwan are larger than the forecasting values.

240

241   Figure 4 shows the verifications generated by the APHR to quantitatively evaluate the performance

242   of the forecasting seismic intensity. We considered the denominator of two classifications in Eq.

243   3, i.e. the total number of the P-alert stations and the total number of boxes in the research area.

244   The results are indicated by "P-alert" and "Map" in Fig. 4, respectively. While comparing

245   forecasting intensity to recorded value, both cases "forecasting = recorded" and "forecasting =

246   recorded +1" belong to "successful forecasting". The definition of the tolerance range that depends

247   on the perspectives and allowance of different users is certainly debatable (Hsu et al., 2018). In

248   our case, the reason is that considering to prevent or mitigate earthquake disaster, "overestimation"

249   is better than "underestimation". Therefore, we tolerated the case of overestimation of 1 intensity

14

Natural Hazards
and Earth System
Sciences
Open Access
Discussions
EGU

250   rather than underestimation.

251

252   First, all red lines are above the maximum hit rate of random tests and higher than 0.5, not to

253   mention the random guess of the eight choices of the seismic intensity scale. It means that these

254   forecasting seismic intensity maps have considerable effectiveness in the forecast, and their good

255   performance can't merely happen by chance. Moreover, another property is that both hit rates of

256   the "P-alert" cases are higher than the rates of the "map" cases. This result could be attributed to

257   the influence of the artificial effect generated by the interpolation of seismic intensity from the P-

258   alert data of nonuniform distribution. Last, it is emphasized that we just focus on the earthquakes

259   with $M_L \geq 5$ in this research, but we cannot deny the possibility of a $M_L < 5$ earthquake to cause

260   large seismic intensity in the near field.

261

262   **5   Discussion**

263   The results of the APHR performance test indicates that the maps and stations of forecasting max

264   seismic intensity by the real-time PSHA are significant and effective. Figure 5 is a concretization

265   of the APHR verification and further gives more details. It clearly shows the P-alert station

266   distributions of the "hit" and "not hit", considering only the station-to-station prediction

267   relationship between the forecasts and records. In both cases, most of the P-alert stations are hit

15

Natural Hazards
and Earth System
Sciences

Discussions

EGU

268   (Fig. 5a and 5b), and the hit percentages distribute along the diagonal and tolerant ranges (Fig. 5c

269   and 5d). However, there still are some locations or stations with wrong forecast. In the case of

270   2016 Meinong earthquake, the stations located in the southwestern Taiwan do not match the real

271   records, and at high seismic intensities (>3), the forecasting results at some stations are

272   underestimated (Fig. 5c), especially in the southwestern area. In the case of 2018 Hualien

273   earthquake, the result from the "P-alert" APHR seems better than former, and further the

274   distribution of the hit percentage is more concentrated along the diagonal and tolerant ranges.

275   Nevertheless, the stations in the southern and part of southwestern Taiwan are still missed. These

276   abovementioned differences between forecasting results and recorded seismic intensities in both

277   cases can be mainly attributed to three aspects.

278

279   First of all, the forecasting model that determines the probability distributions of earthquake

280   occurrences is critical for the real-time PSHA. If the probability distribution is missing or false

281   alarm in somewhere, it directly causes the inaccurate forecasts to the real-time PSHA. In the PI

282   results, some differences are located on the hotspots with relatively higher probability, for example,

283   the area in 22.6º to 23ºN and 120.9º to 121.3ºE in Fig. 1a, and 22.7º to 23.1ºN and 120.4º to 120.8ºE

284   in Fig. 1b. Compared the locations of the earthquakes, these hotspots just shift slightly and it seems

285   acceptable. However, in the results of the real-time PSHA, it leads the maps of forecasting max

286   seismic intensity to underestimate in the area near the epicenters and overestimate in the area

287   without any earthquake event, but with high probability of earthquake occurrence. For instance,

288   the southwestern area in the case of 2018 Hualien earthquake is underestimated because of this

289   reason, and then it also causes overestimated in the southern area (see Fig. 3 and 5b). Therefore, a

290   more accurate and precise forecasting model helps us get a more positive result in a real-time

291   PSHA. Even if the PI results perform well in the ROC test, the PI method still needs to be improved.

292

293   Secondly, the evaluation of earthquake ground motion suffers from the limitations of GMPEs. We

294   adopted the GMPE produced by Lin et al. (2012) whose data ($M_L \geq 5.0$) within 50 km are less than

295   14% of all data for the regression of GMPE. If there is a shortage of data in near field and for larger

296   events in the regression of GMPEs, the applicability of GMPEs is limited (Edwards and Fäh, 2014).

297   Therefore, that probably causes the deviation of evaluation on forecasting seismic intensity maps,

298   for instance, the underestimation of the areas around the two main shocks (Fig. 2c and 3c).

299   Moreover, the site effect is difficult to be properly and comprehensively evaluated in GMPEs, but

300   it dramatically affects the behavior of seismic waves. For example, the amplitudes in the Meinong

301   earthquake were amplified extending along the northwest (in Fig. 2b) because of the Western Plain

302   composed of thick and low velocity sedimentary deposits (see Fig. 4 in Lee et al., 2016). As a

303   result, the site effect also contributes and leads the seismic intensity forecast to underestimate (Fig.

Natural Hazards
and Earth System
Sciences
Discussions
Open Access
EGU

304   2c and 5a).

305

306   Last but not least, the directivity effect also plays an important role in the distribution of ground

307   motion. For the main shocks in two cases, the rupture characteristic brings a strong directivity

308   effect that causes the significant amplification of ground motion along the rupture direction (Lee

309   et al., 2016; Hsu et al., 2018). However, GMPEs are basically a statistical distribution of PGA

310   generated by all data at the same radical distance without considering possible effect of rupture

311   directivity. As a result, GMPEs are only able to provide the ground motion estimation of radial

312   extension. Besides, the forecasting model does not include the information of rupture direction

313   either. Therefore, we suggest that some differences which along the rupture direction may belong

314   to this effect.

315

316   **6   Conclusion**

317   This study presents how the real-time seismic hazard assessment can be achieved by replacing the

318   static seismic rate, i.e. the truncated and characteristic earthquake models, with the time-dependent

319   seismic source probability of the PI method. With regard to the time-dependent seismic source

320   probability, the ROC tests verified quantitatively that the performances of the PI forecasting

321   probabilities in forecasting interval are quite effective. Therefore, those significant probability

322   distributions can be used as the function of earthquake occurrence rate, $P(m, loc)$, in the real-time

323   PSHA. Our forecasting seismic intensity maps of the real-time PSHA have the hit rates

324   outperformed the random guesses and higher than 0.5 for both cases of the Meinong and Hualien

325   earthquakes. This study thus suggests that these real-time PSHA maps are effective in terms of

326   forecasting, and their good performances are not likely coincidence. We demonstrated that the real-

327   time seismic hazard assessment is doable and can be realized and updated by the time-dependent

328   seismic source probability.

329

330   In the future, the different time-dependent seismic source probability models can be introduced to

331   provide a more accurate and robust estimation for earthquake occurrences. Also, a possible

332   improvement for our results could be from the estimated PGA distribution not only by means of

333   the state-of-the-art machine learning tools for a big data bank of the P-alert network but also by

334   physics-based numerical simulations (PBS) of seismic ground motion, instead of the empirical

335   GMPEs. Presumably, a real-time forecasting map of seismic intensity enables governments or

336   businesses to efficiently prepare for earthquake disasters. Moreover, the seismicity intensity scale

337   based on PGA are related to the vulnerability level of buildings, which will also be changed with

338   time due to the degradation and upgrades (e.g. obsolescence, retrofitting actions, climate events).

339   Therefore, when further assessing a seismic risk fluctuating with time, the real-time PSHA and the

340   change of vulnerability should be considered.

341

342   **Acknowledgments**

348

349   **References**

350   Chang, L.-Y., Chen, C.-c., Wu, Y.-H., Lin, T.-W., Chang, C.-H., and Kan, C.-W.: A Strategy for

351   a Routine Pattern Informatics Operation Applied to Taiwan, Pure Appl. Geophys., 173, 235-

352   244, doi:10.1007/s00024-015-1079-9, 2016.

353   Chang, L.-Y.: A study on an improved pattern informatics method and the soup-of-group model

354   for earthquakes. Doctoral dissertation, Department of Earth Sciences, National Central

355   University, Taiwan, R. O. C., 2018.

356   Chen, C.-c., Rundle, J. B., Holliday, J. R., Nanjo, K. Z., Turcotte, D. L., Li, S.-C., and Tiampo, K.

357   F.: The 1999 Chi-Chi, Taiwan, earthquake as a typical example of seismic activation and

358   quiescence, Geophys. Res. Lett., 32, L22315, doi:10.1029/2005GL023991, 2005.

359   Chen, C.-c., Rundle, J. B., Li, H.-C., Holliday, J. R., Turcotte, D. L., and Tiampo, K. F.: Critical

360   point theory of earthquakes: Observation of correlated and cooperative behavior on

361   earthquake fault systems, Geophys. Res. Lett., 33, L18302, doi:10.1029/2006GL027323,

362   2006.

363   Chen, H.-J., Chen, C.-c., Ouillon, G., and Sornette, D.: Using geoelectric field skewness and

364   kurtosis to forecast the 2016/2/6, M L 6.6 Meinong, Taiwan Earthquake, Terr. Atmos. Ocean.

365   Sci., 28, 745-761, doi:10.3319/TAO.2016.11.01.01, 2017.

366   Cooper, J. D.: Letter to editor, San Francisco Daily Evening Bulletin, Nov. 3, 1868.

367   Cornell, C. A.: Engineering seismic risk analysis, Bull. Seismol. Soc. Am., 58, 1583-1606, 1968.

368   Cosentino, P., Ficarra, V., and Luzio, D.: Truncated exponential frequency-magnitude relationship

369   in earthquake statistics, Bull. Seismol. Soc. Am., 67, 1615-1623, 1977.

370   Edwards, B., and Fäh, D.: Ground motion prediction equations, ETH-Zürich, 2014.

371   Holliday, J. R., Rundle, J. B., Turcotte, D. L., Klein, W., Tiampo, K. F., and Donnellan, A.: Space-

372   Time Clustering and Correlations of Major Earthquakes, Phys. Rev. Lett., 97, 238501,

373   doi:10.1103/PhysRevLett.97.238501, 2006.

374   Gutenberg, B. and Richter, C. F.: Frequency of earthquakes in California, Bull. Seism. Soc. Am.,

375   34, 185–188, 1944.

376   Hsu, T. Y., Lin, P. Y., Wang, H. H., Chiang, H. W., Chang, Y. W., Kuo, C. H., Lin, C. M., and

377   Wen, K. L.: Comparing the Performance of the NEEWS Earthquake Early Warning System

378   Against the CWB System During the 6 February 2018 Mw 6.2 Hualien Earthquake, Geophys.

379   Res. Lett., 45, 6001-6007, doi:10.1029/2018GL078079, 2018.

380   Iervolino, I., Chioccarelli, E., and Convertito, V.: Engineering design earthquakes from

381   multimodal hazard disaggregation, Soil Dynam. Earthquake Eng., 31, 1212-1231,

382   https://doi.org/10.1016/j.soildyn.2011.05.001, 2011.

383   Lee, S.-J., Yeh, T.-Y., and Lin, Y.-Y.: Anomalously Large Ground Motion in the 2016 ML 6.6

384   Meinong, Taiwan, Earthquake: A Synergy Effect of Source Rupture and Site Amplification,

385   Seismol. Res. Lett., 87, 1319-1326, doi:10.1785/0220160082, 2016.

386   Lee, Y.-T., Wang, Y.-J., Chan, C.-H., and Ma, K.-F.: The 2016 Meinong earthquake to TEM

387   PSHA2015, Terr. Atmos. Ocean. Sci., 28, 703-713, doi:10.3319/TAO.2016.12.28.02, 2017.

388   Lin, P.-S., Hsie, P.-S., Lee, Y.-R., Cheng, C.-T., and Shao, K.-S.: The research of probabilistic

389   seismic hazard analysis and geological survey of nuclear power plant: Construction of ground

390   motion prediction equation for response spectra., Commission Report of the Institute of

391   Nuclear Energy Research, Atomic Energy Council, Executive Yuan. (in Chinese), 2012.

392   Nanjo, K. Z., Holliday, J. R., Chen, C.-c., Rundle, J. B., and Turcotte, D. L.: Application of a

393   modified pattern informatics method to forecasting the locations of future large earthquakes

Natural Hazards
and Earth System
Sciences
Discussions

Open Access

EGU

394 in the central Japan, Tectonophysics, 424, 351-366,

395   https://doi.org/10.1016/j.tecto.2006.03.043, 2006.

396 Rundle, J. B., Klein, W., Tiampo, K., and Gross, S.: Linear pattern dynamics in nonlinear threshold

397   systems, Phys. Rev. E, 61, 2418-2431, doi:10.1103/PhysRevE.61.2418, 2000.

398 Rundle, J. B., Tiampo, K. F., Klein, W., and Sá Martins, J. S.: Self-organization in leaky threshold

399   systems: The influence of near-mean field dynamics and its implications for earthquakes,

400   neurobiology, and forecasting, Proc. Nat. Acad. Sci., 99, 2514-2521,

401   doi:10.1073/pnas.012581899, 2002.

402 Rundle, J. B., Turcotte, D. L., Shcherbakov, R., Klein, W., and Sammis, C.: Statistical physics

403   approach to understanding the multiscale dynamics of earthquake fault systems, Rev.

404   Geophys., 41, 1019, doi:10.1029/2003RG000135, 2003.

405 Senior Seismic Hazard Analysis Committee (SSHAC): Recommendations for probabilistic

406   seismic hazard analysis: guidance on uncertainty and use of experts, US Nuclear Regulatory

407   Commission Washington, DC, 1997.

408 Schwartz, D. P., and Coppersmith, K. J.: Fault behavior and characteristic earthquakes: Examples

409   from the Wasatch and San Andreas Fault Zones, J. Geophys. Res., 89, 5681-5698,

410   doi:10.1029/JB089iB07p05681, 1984.

411 Sharda, R., and Delen, D.: Predicting box-office success of motion pictures with neural networks,

412   Expert Syst. Appl., 30, 243-254, https://doi.org/10.1016/j.eswa.2005.07.018, 2006.

413   Shyu, J. B. H., Chuang, Y.-R., Chen, Y.-L., Lee, Y.-R., and Cheng, C.-T.: A New On-Land

414   Seismogenic Structure Source Database from the Taiwan Earthquake Model (TEM) Project

415   for Seismic Hazard Analysis of Taiwan, Terr. Atmos. Ocean. Sci., 27, 311-323,

416   doi:10.3319/TAO.2015.11.27.02(TEM), 2016.

417   Tiampo, K. F., Rundle, J. B., McGinnis, S., Gross, S. J., and Klein, W.: Mean-field threshold

418   systems and phase dynamics: An application to earthquake fault systems, Europhys. Lett., 60,

419   481, doi:10.1209/epl/i2002-00289-y, 2002.

420   Wang, J.-H., Chen, K.-C., Leu, P.-L., and Chang, J.-H.: b-Values Observations in Taiwan: A

421   Review, Terr. Atmos. Ocean. Sci., 26, 475-492, doi:10.3319/TAO.2015.04.28.01(T), 2015.

422   Wang, Y.-J., Chan, C.-H., Lee, Y.-T., Ma, K.-F., Shyu, J. B. H., Rau, R.-J., and Cheng, C.-T.:

423   Probabilistic Seismic Hazard Assessment for Taiwan, Terr. Atmos. Ocean. Sci., 27, 325-340,

424   doi:10.3319/TAO.2016.05.03.01, 2016.

425   Wu, Y.-M., Shin, T.-C., and Tsai, Y.-B.: Quick and reliable determination of magnitude for

426   seismic early warning, Bull. Seismol. Soc. Am., 88, 1254-1259, 1998.

427   Wu, Y.-M., Teng, T.-l., Shin, T.-C., and Hsiao, N.-C.: Relationship between Peak Ground

428   Acceleration, Peak Ground Velocity, and Intensity in Taiwan, Bull. Seismol. Soc. Am., 93,

429   386-396, doi:10.1785/0120020097, 2003.

430   Wu, Y.-H., Chen, C.-c., and Rundle, J. B.: Detecting precursory earthquake migration patterns

431   using the pattern informatics method, Geophys. Res. Lett., 35, L19304,

432   doi:10.1029/2008GL035215, 2008a.

433   Wu, Y.-H., Chen, C.-c., and Rundle, J. B.: Precursory seismic activation of the Pingtung (Taiwan)

434   offshore doublet earthquakes on 26 December 2006: A pattern informatics analysis, Terr.

435   Atmos. Ocean. Sci., 19, 743-749, doi:10.3319/TAO.2008.19.6.743(PT), 2008b.

436   Wu, Y.-M., Chang, C.-H., Zhao, L., Teng, T.-L., and Nakamura, M.: A Comprehensive Relocation

437   of Earthquakes in Taiwan from 1991 to 2005, Bull. Seismol. Soc. Am., 98, 1471-1481,

438   doi:10.1785/0120070166, 2008c.

439   Wu, Y.-M., Chen, D.-Y., Lin, T.-L., Hsieh, C.-Y., Chin, T.-L., Chang, W.-Y., and Li, W.-S.: A

440   High-Density Seismic Network for Earthquake Early Warning in Taiwan Based on Low Cost

441   Sensors, Seismol. Res. Lett., 84, 1048-1054, doi:10.1785/0220130085, 2013.

442   Wu, Y.-H., Chen, C.-c., and Li, H.-C.: Conditional Probabilities for Large Events Estimated by

443   Small Earthquake Rate, Pure Appl. Geophys., 173, 183-196, doi:10.1007/s00024-014-1019-

444   0, 2016a.

445   Wu, Y.-M., Liang, W.-T., Mittal, H., Chao, W.-A., Lin, C.-H., Huang, B.-S., and Lin, C.-M.:

446   Performance of a Low-Cost Earthquake Early Warning System (P-Alert) during the 2016 ML

447   6.4   Meinong   (Taiwan)   Earthquake,   Seismol.   Res.   Lett.,   87,   1050-1059,
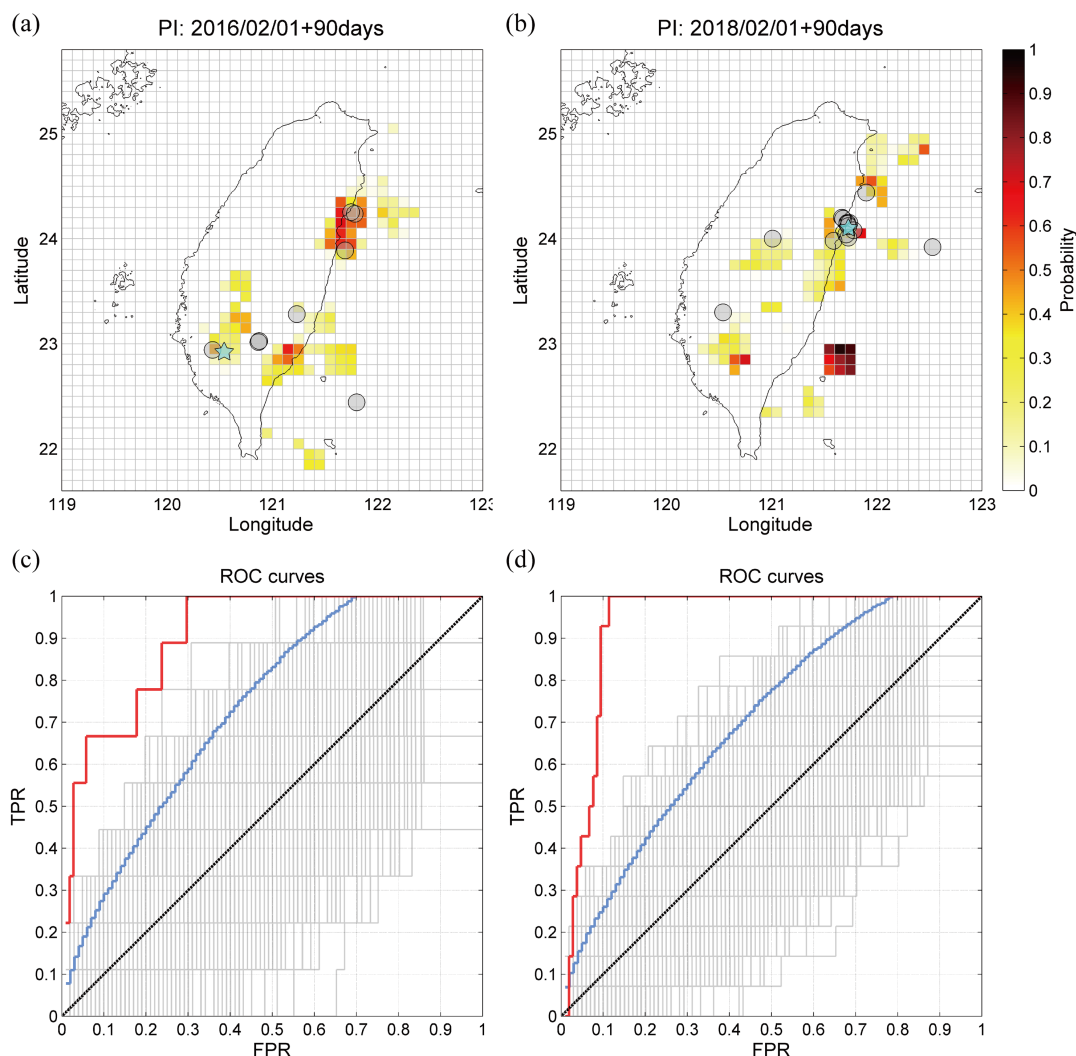
448   doi:10.1785/0220160058, 2016b.

449   Yang, B. M., Huang, T.-C., and Wu, Y.-M.: ShakingAlarm: A Nontraditional Regional Earthquake

450   Early Warning System Based on Time-Dependent Anisotropic Peak Ground-Motion

451   Attenuation   Relationships,   Bull.   Seismol.   Soc.   Am.,   108,   1219-1230,

452   doi:10.1785/0120170105, 2018.

Figure 1. Panels (a) and (b) show the forecasting probability maps of the Meinong earthquake and the Hualien earthquake, respectively. Panels (c) and (d) are the ROC curves of (a) and (b), respectively. Red, gray, blue, and black curve represent the forecasting probability map, random tests, 95% confidence interval, and the average of random tests, respectively.

453

454

455

456

457

458
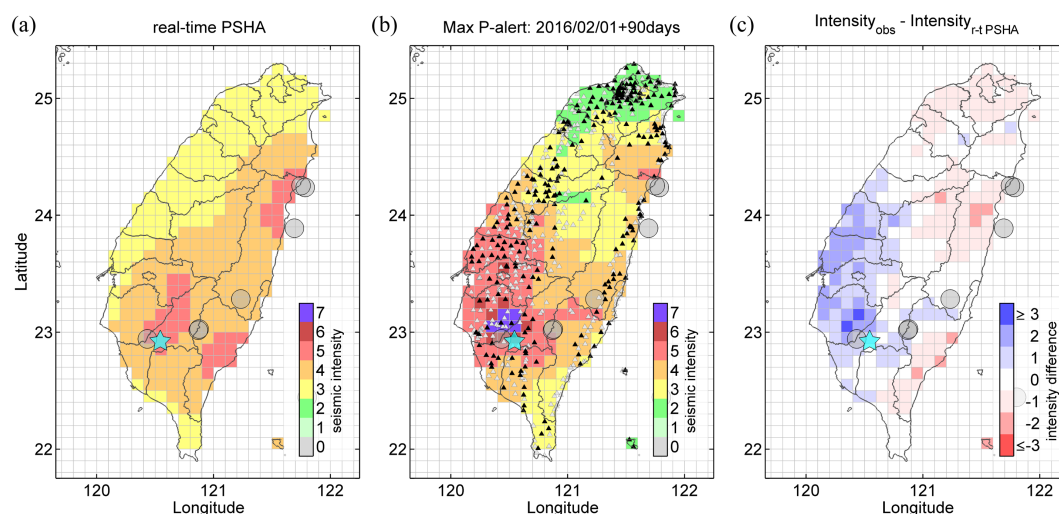
Figure 2. The case of 2016 Meinong earthquake: (a) The map of forecasting max seismic intensity by the rea-time PSHA. The forecasting interval of seismic intensity is 90 days. (b) The map of max seismic intensity recorded by the P-alert network. Black and white triangles indicate the P-alert stations which we used and didn't use in the verification, respectively. (c) The difference of seismic intensity between the forecast and the record. Cyan star represents the Meinong earthquake; gray circles represent the earthquakes with magnitude $M_L \geq 5$ in this forecasting interval.

471
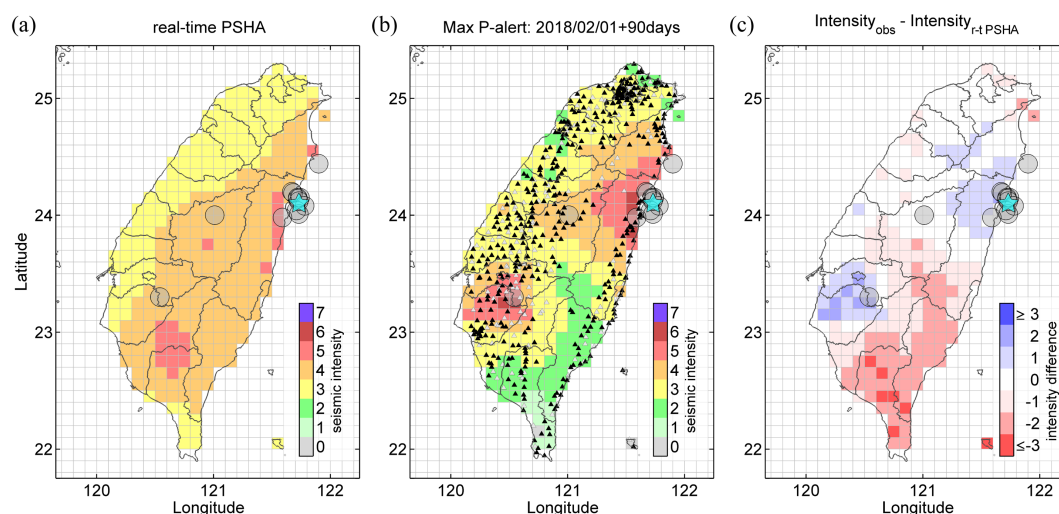

Figure 3. The case of 2018 Hualian earthquake: (a) The map of forecasting max seismic intensity.
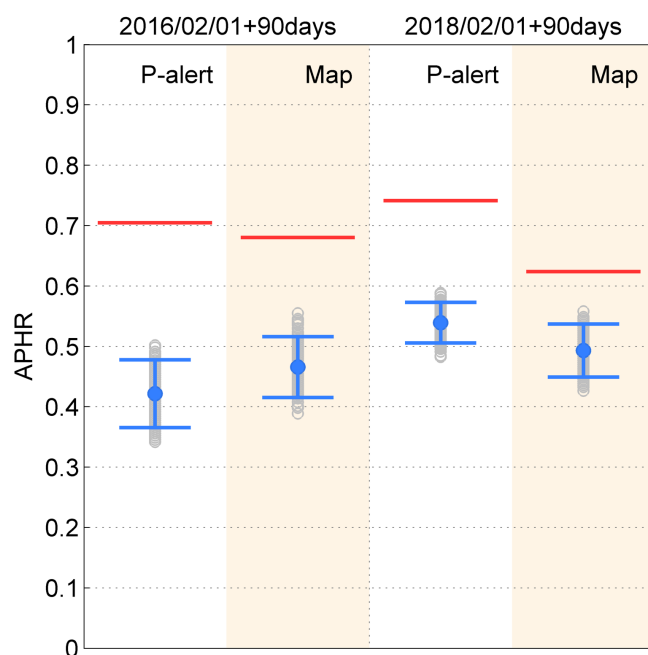
473   (b) The map of max seismic intensity recorded by the P-alert network. (c) The difference of seismic

474   intensity between the forecast and the record. Cyan star represents the Hualian earthquake.

475

476

477

Natural Hazards
and Earth System
Sciences
Discussions

Open Access

EGU

478

479   Figure 4. Performance test of APHR. Red line indicates the forecasts of the real-time PSHA; gray

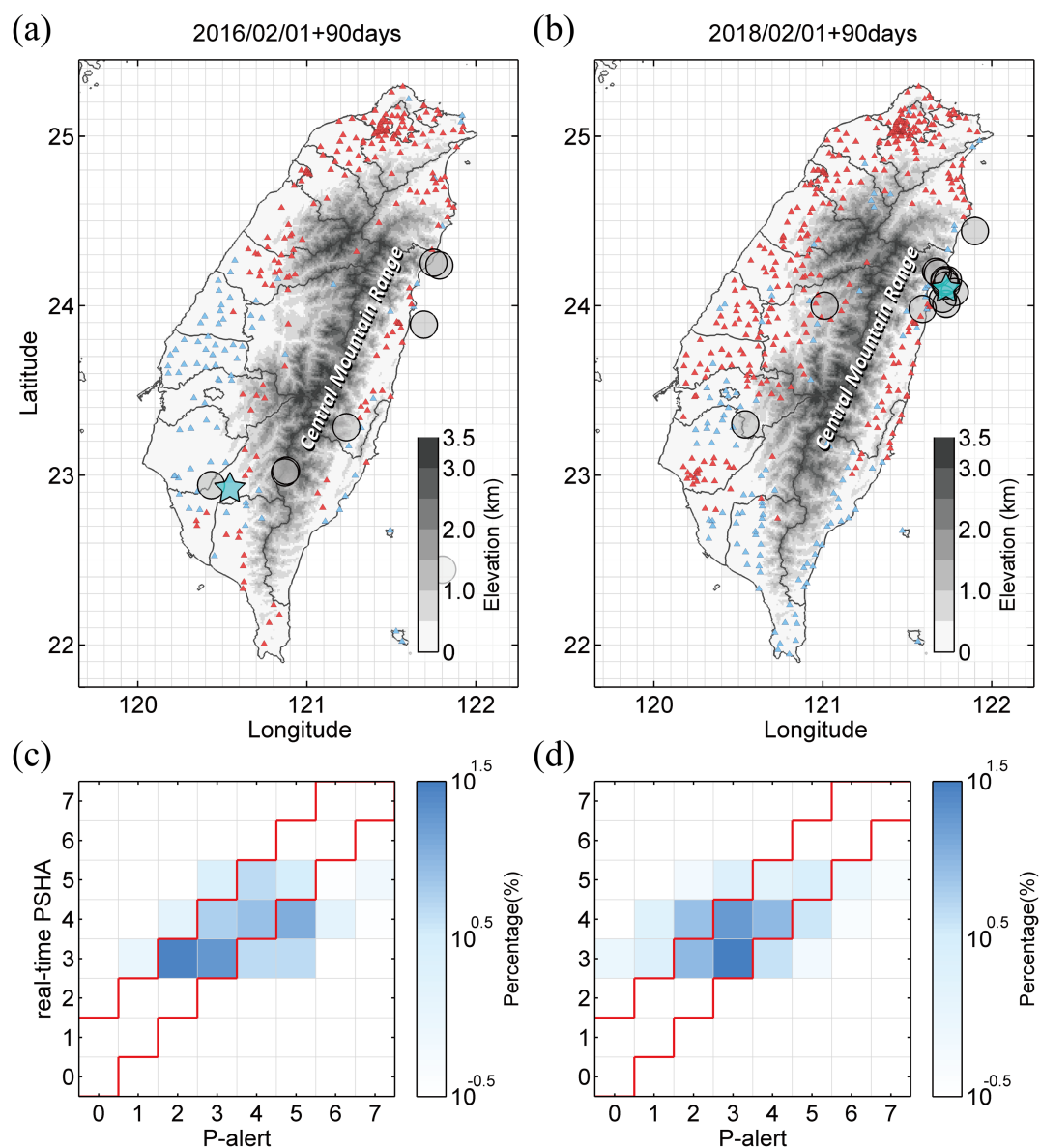480   circle indicates the result of a random test by randomly re-distributing seismic intensities; blue

481   error bar indicates the interval with two standard deviations over all random tests.

482

483

484

485

Figure 5. Panels (a) and (b) are the P-alert station distributions of the "hit" and "not hit". Red and

blue triangles present the "hit" and "not hit", respectively. Panels (c) and (d) are the distributions

of the hit percentage for the cases of 2016 Meinong and 2018 Hualian earthquake, respectively.

490   Red line area presents the acceptable prediction range.

491

Natural Hazards
and Earth System
Sciences
Discussions

Open Access

EGU

492   Table 1. The earthquakes occurred in the forecast interval. "P-alert" indicates that the P-alert

493   recording obtained from the Taiwan Earthquake Research Center (TEC) or the National Taiwan

494   University (NTU). "Num." is the number of recording stations. "Nan" indicates that there is no P-

495   alert data to be recorded in both TEC and NTU even if that event was recorded by CWB. The bold

496   represents the Meinong and Hualian earthquakes.

(a) Meinong case: 2016/02/01~2016/05/01

Date	Hour	Min.	Lon.	Lat.	Depth	M_L	P-alert	Num.
02/05	**19**	**57**	**120.54**	**22.92**	**14.64**	**6.60**	**TEC**	**338**
02/05	19	58	120.43	22.94	18.10	5.26	Nan	Nan
02/09	00	47	121.69	23.89	5.69	5.12	TEC	341
02/18	01	09	120.87	23.02	5.44	5.27	TEC	357
02/18	01	18	120.88	23.03	4.26	5.13	TEC	357
04/16	10	55	121.80	22.44	11.83	5.22	TEC	436
04/27	15	17	121.78	24.24	11.94	5.67	NTU	424
04/27	15	27	121.75	24.25	12.99	5.13	NTU	425
04/27	18	19	121.23	23.28	15.21	5.52	NTU	423

497

(b) Hualian case: 2018/02/01~2018/05/02

Date	Hour	Min.	Lon.	Lat.	Depth	M_L	P-alert	Num.
02/04	13	12	121.67	24.20	15.10	5.10	TEC	543
02/04	13	56	121.74	24.15	10.60	5.80	TEC	519
02/04	13	57	121.68	24.19	11.10	5.10	Nan	Nan
02/04	14	13	121.72	24.15	10.30	5.50	TEC	517
02/05	15	58	121.72	24.14	10.00	5.00	TEC	522
02/06	**15**	**50**	**121.73**	**24.10**	**6.30**	**6.20**	**TEC**	**520**
02/06	15	53	121.59	23.98	5.10	5.00	TEC	520

Natural Hazards
and Earth System
Sciences
Open Access
EGU
Discussions

02/06	18	00	121.73	24.12	6.70	5.30	TEC	516
02/06	18	07	121.71	24.04	4.20	5.30	TEC	516
02/06	19	15	121.73	24.01	5.70	5.40	TEC	516
02/07	15	21	121.78	24.08	7.80	5.80	TEC	523
02/25	18	28	121.90	24.44	17.70	5.20	TEC	533
03/20	09	22	120.54	23.30	11.20	5.30	TEC	539
03/29	00	17	121.01	24.00	11.10	5.00	NTU	388
04/23	17	10	122.53	23.92	19.30	5.10	NTU	381

498

499   Table 2. Seismic intensity scale of CWB.

Intensity Scale		Ground Acceleration (cm/s^2, gal)
Micro	0	<0.8
Very minor	1	0.8~2.5
Minor	2	2.5~8.0
Light	3	8~25
Moderate	4	25~80
Strong	5	80~250
Very Strong	6	250~400
Great	7	≥400

500